PHYSICAL REVIEW B **80**, 125208 (2009)

Antimony as an amphoteric dopant in lead telluride

Christopher M. Jaworski,[1] Janusz Tobola,[2] E. M. Levin,[3,4] Klaus Schmidt-Rohr,[3,5] and Joseph P. Heremans[1,6]
[1]*Department of Mechanical Engineering, The Ohio State University, Columbus, Ohio 43210, USA*
[2]*Faculty of Physics and Applied Computer Science, AGH University of Science and Technology, 30-059 Krakow, Poland*
[3]*Ames Laboratory DOE, Ames, Iowa 50011, USA*
[4]*Department of Physics and Astronomy, Iowa State University, Ames, Iowa 50011, USA*
[5]*Department of Chemistry, Iowa State University, Ames, Iowa 50011, USA*
[6]*Department of Physics, The Ohio State University, Columbus, Ohio 43210, USA*

(Received 26 May 2009; revised manuscript received 3 August 2009; published 24 September 2009)

We elucidate the amphoteric nature of antimony as a dopant in PbTe. Band-structure calculations show that Sb substituting for Pb is a donor and that Sb on the Te site is an acceptor giving rise to a large excess density of states (DOS). Experimentally, in Te-rich $Pb_{1-x}Sb_xTe$ samples, ^{125}Te NMR spectroscopy shows that Sb substitutes for Pb and transport data reveal that it then acts as a simple donor. In Pb-rich $PbSb_xTe_{1-x}$ samples, ^{125}Te NMR shows that little Sb substitutes for Te when samples are prepared above 770 K and then quenched; ^{207}Pb NMR shows four types of charge carriers, but only a majority hole and a minority electron contribute to transport. Sb acts as an acceptor in $PbSb_xTe_{1-x}$, but the large DOS calculated must correspond to a large concentration of localized holes and the Seebeck coefficient is not enhanced.

DOI: 10.1103/PhysRevB.80.125208 PACS number(s): 84.60.Rb, 76.60.−k, 71.15.Qe

I. INTRODUCTION

Lead telluride is a compound semiconductor commonly used in thermoelectric power generation from heat sources around 770 K such as produced by combustion processes or encountered in waste heat recovery applications. The thermoelectric figure of merit of PbTe, $zT=TS^2\sigma/\kappa$, where T is the average temperature and S the Seebeck coefficient while σ and κ are the electrical and thermal conductivity, is typically limited to 0.7 for p-type material and 1.1 for n-type material. Recently, several PbTe-based material systems have been identified that have $zT>1$,[1] some of which are based on antimony-containing PbTe such as $AgPb_{18}SbTe_{20}$ (Ref. 2) and PbTe+Pb/Sb.[3] The conclusions we will reach here may also shed light on the behavior of other antimony-containing semiconductor chalcogenides that have important thermoelectric applications such as Sb_2Te_3 and $AgSbTe_2$.

The behavior of antimony in PbTe has long been known to be complex. Indeed, Strauss[4] indicates in 1973 that Sb appears to be amphoteric in PbTe but states that the evidence is not conclusive. He reports conduction to be p type or n type as a function of whether the material is lead or tellurium rich and of the annealing temperature. Lead-rich Sb-doped samples, as grown or annealed at 1073 K are n type, while those saturated at 773 K are n type at 77 K while p type at 300 K. Tellurium-rich Sb-doped samples saturated at 623 K are n type while those annealed at 1073 K are p type. Strauss attributes this amphoteric behavior to the ability of Sb to occupy two different lattice sites. The purpose of this study is to investigate the role of Sb in PbTe and to establish both theoretically and experimentally that it is a donor when it substitutes Pb and an acceptor when substituting for Te.

We present band-structure calculations that indicate that Sb can act as either a donor or an acceptor in PbTe. When Sb is placed on the metal sites, its energy level lies just above the Fermi level and it donates electrons to the lattice. When Sb is placed on the chalcogen site, its energy level lies just below the Fermi energy and slightly off of the Pb and Te energy levels. Here, antimony will act as an acceptor. In order to ascertain the role of antimony experimentally in these compounds and verify the band-structure calculations, we prepare PbTe samples in which we attempt to place Sb on either the metal or the chalcogenide lattice sites of PbTe. The nominal compositions of $x=0.25\%$ (=0.0025), 0.5%, and 1% Sb (with either Pb or Te at unity and the other at 1-x) were chosen as to stay within the solubility range[5] of Sb in PbTe while at the same time introducing enough Sb into the lattice to allow for conclusive evidence to be collected. In addition to transport measurements, ^{125}Te and ^{207}Pb NMR with magic-angle spinning was used to probe the local composition and charge-carrier concentration.

II. THEORY

Electronic structure calculations of disordered NaCl-type structure $Pb_{1-x}Sb_xTe$ and $PbSb_xTe_{1-x}$ alloys have been performed using the Green function Korringa-Kohn-Rostoker method with the use of the coherent potential approximation (KKR-CPA) to treat chemical disorder.[6,7] In all computations, the room temperature experimental value of lattice constant ($a=6.462$ Å)[8] was used. The self-consistent crystal potential of muffin-tin form was constructed with the LDA framework, using the von Barth-Hedin formula for the exchange-correlation part. We restricted the KKR-CPA computations in doped PbTe samples to only the spherical part of the potential; to verify the validity of this hypothesis, we have also employed the full-potential KKR method to compute the electronic structure of ordered PbTe, where the full form of the crystal potential over the whole atomic Voronoi cells was applied, with l truncation on each atom up to $l_{max}=3$. For finally converged atomic charges below $10^{-3}q$ and potentials below 1 mRy, the total, site-decomposed, and l-decomposed density of states (DOSs) were computed using the integration tetrahedron method in reciprocal space

(550 k-space points in the irreducible part of the Brillouin zone). The Fermi level (E_F) was precisely determined from the Lloyd method,[9] which appears to be particularly important in systems close to the semiconductor-metal limit. In all figures presented here, E_F is located at zero and nonspin-polarized DOS curves are given in Ry^{-1} per spin direction. The core states were calculated fully relativistically, whereas the valence states were treated in a nonrelativistic approach. Notably, previous theoretical studies of electronic structure of PbTe (Refs. 10 and 11) revealed that this compound exhibited a direct energy gap (E_g) at the L point in the Brillouin zone and relativistic effects were important to correctly reproduce the experimental energy gap (~ 0.2 eV). It was also shown[10,11] that the inclusion of spin-orbit interactions into the computations did not markedly change the character of bands in the vicinity of valence and conduction-band edges but it strongly decreased the E_g value. Consequently, semirelativistic LDA computations without spin-orbit corrections[10] yielded a much larger direct energy gap ~ 0.65 eV at L point. Bearing in mind the influence of spin-orbit interaction on the energy gap, we focus mainly on the effect of Sb doping on the electronic structure of PbTe, when diluting antimony on either Pb or Te sites. We expect that relativistic effects, neglected in this study, inevitably decrease the energy gap in disordered $\mathrm{Pb}_{1-x}\mathrm{Sb}_x\mathrm{Te}$ and $\mathrm{PbSb}_x\mathrm{Te}_{1-x}$ samples, but they should not substantially change the position of Sb-DOS peaks with respect to electronic states near the valence and conduction edges of pure PbTe. The analysis presented here is based on the semirelativistic KKR-CPA predictions, which appear very useful in qualitative interpretations of our electron transport measurements.

A. PbTe

The density of states of pure PbTe is shown in Fig. 1, where one can identify five valence bands (not shown) lying below the Fermi level. Two of these bands form separate s-like bands in lower-energy range: the lowest band, shown in Fig. 1(c), is mainly attributed to Te s states, whereas the higher lying one, shown in Fig. 1(b), corresponds in principle to Pb s states. This interesting separation of s-like bands in PbTe compound can be roughly related to significant differences in atomic potentials of Pb (group IV) and Te (group VI), arising from a particular interplay between interatomic distances and a difference in atomic number of constituent elements.

The higher lying block of bands is ascribed to Pb and Te p states with a small admixture of Pb s states (Fig. 1(b)), producing the Pb-DOS peak below E_F. The contribution of Pb s states in formation of electronic structure below the band gap can also be detected on Pb-DOSs in $\mathrm{Pb}_{1-x}\mathrm{Sb}_x\mathrm{Te}$ and $\mathrm{PbTe}_{1-x}\mathrm{Sb}_x$ (see below in Figs. 2 and 3, respectively). A strong hybridization of Pb p states (dominating unoccupied conduction bands) and Te p states (building mostly occupied valence bands) results in an energy gap at the Fermi level. The KKR value of $E_g = 0.68$ eV remains in good agreement with recent linear augmented plane wave (LAPW) calculations[10] and, as mentioned above, is much larger than the optical value (~ 0.2 eV). Finally, from the DOS of PbTe one can notice quite different DOS variations near the valence (larger) and conduction-band edges; interestingly, we note that experimentally the dependence of the Seebeck coefficient on carrier concentration is almost the same in conventially doped n-type and p-type PbTe.

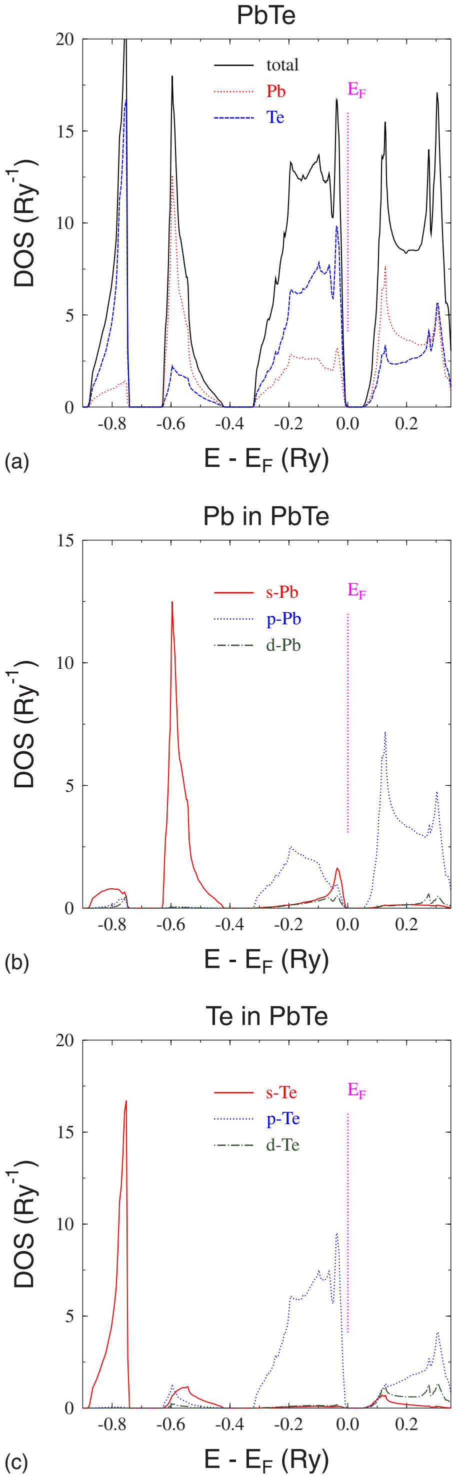

FIG. 1. (Color online) Total (a) and site-decomposed (b, c) DOS of pure PbTe as function of energy. The Fermi level is set on this diagram at 0 Ry.

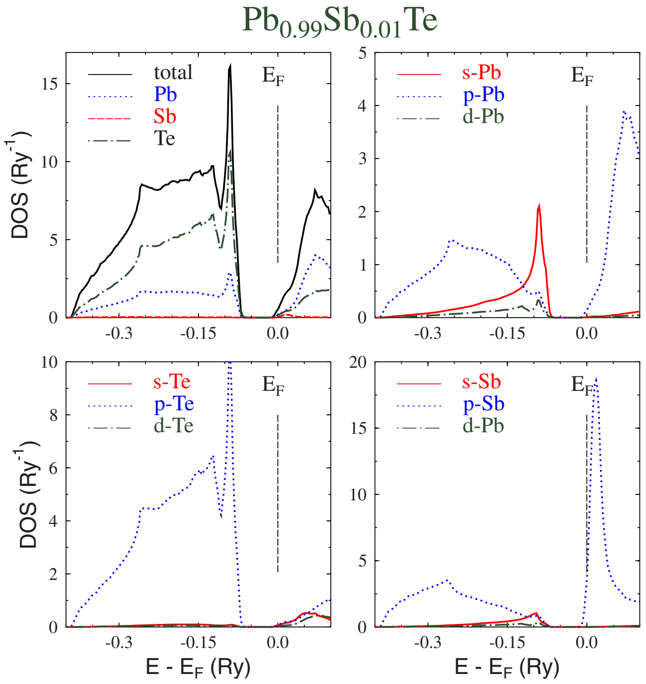

FIG. 2. (Color online) Density of states of $Pb_{0.99}Sb_{0.01}Te_1$ as a function of energy (in the top left panel atom DOS is multiplied by concentration, while in other panel DOS is given per atom).

B. $Pb_{1-x}Sb_xTe$

Figure 2 presents the calculated DOS in $Pb_{0.99}Sb_{0.01}$ Te alloy, assuming that antimony substitutes for lead. It is intuitive to expect that trivalent Sb donating one extra electron to the system should behave as an electron donor. Indeed, Sb creates a large *p*-DOS peak at the bottom of the conduction band, since five valence bands are already complete. E_F lies on the increasing DOS slope which is in line with negative thermopower observed in $Pb_{1-x}Sb_xTe$. This large DOS peak from Sb may markedly modify the total DOS even at low antimony contents. Hence, electronic structure changes upon Sb doping on Pb site should not rigorously be interpreted in terms of a simple rigid band model, but still Sb on a Pb site does not noticeably reduce the energy gap. As expected, Sb *p* states are also observed in the valence band and the antimony contribution is comparable to that of lead. Strong overlap of *p* states from Sb and Pb confirms their bonding character in the energy range below the energy gap. Conversely, the principal Sb-DOS peak occurring at the conduction band edge exhibits a less bonded character.

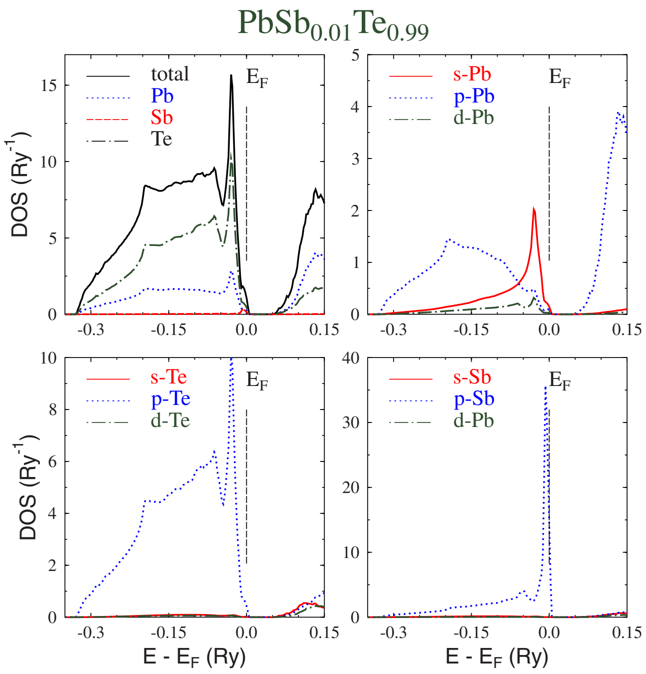

FIG. 3. (Color online) Density of states of $Pb_1Sb_{0.01}Te_{0.99}$ as a function of energy (in the top left panel atom DOS is multiplied by concentration, while in other panel DOS is given per atom).

C. $PbSb_xTe_{1-x}$

Figure 3 presents the DOS in $PbSb_{0.01}Te_{0.99}$ alloy, where antimony is assumed to substitute for tellurium. In this case one might intuitively argue that when a Sb atom of valence five substitutes for a Te atom of valence six, it delivers one electron less to the system than the Te, and could act as an electron acceptor. Indeed, the calculation shows that Sb creates a huge and narrow *p*-DOS peak (more than twice higher than the equivalent one on the Pb site) on the border between the valence-band edge and energy gap. Such a behavior is not fully symmetric to that one seen above in the *n*-doped $Pb_{0.99}Sb_{0.01}Te$, since this Sb peak is partly isolated from valence states of the host. The rigid band predictions practically fail in the case of Sb doping on the Te site. The energy gap is now slightly decreased, unlike the case of $Pb_{0.99}Sb_{0.01}Te$. Moreover, a very weak hybridization of this *p*-Sb peak would indicate its nonbonding character; indeed, we will show experimentally that the Sb level in this condition will accept few and only thermally activated free electrons. On the whole, the Fermi level lies on a strongly decreasing DOS and its position is essentially governed by the antimony concentration. In view of our KKR-CPA results, E_F seems to be almost confined in the Sb *p*-DOS peak and total the DOS of $PbSb_{0.01}Te_{0.99}$ is more strongly dependent on the impurity electronic states than in the case of $Pb_{0.99}Sb_{0.01}Te$. To further illustrate this point, we show the Sb-content dependence of the valence band structure for $PbSb_xTe_{1-x}$, with $x=0,0.01$ and 0.05 in Fig. 4(a). Sb substituting for Te visibly modifies the valence-band edge close to *L* point, even at low concentration. Along *L*-Γ, in particular, this band becomes more flat near *L*, and modifications are also seen along *K*-Γ direction. Moreover, the energy gap slightly decreases, even though we assumed the lattice constant to be independent of Sb content. Comparing this result to the calculated evolution of the bands with Sb concentration in $Pb_{1-x}Sb_xTe$, (Fig. 4(b)), we note that Sb on the Pb-site affects the conduction bands near E_F much less.

III. EXPERIMENTS

Ingots of $Pb_{1-x}Sb_xTe$ and of $PbSb_xTe_{1-x}$ were prepared by mixing stoichiometric amounts of pure lead, antimony, and

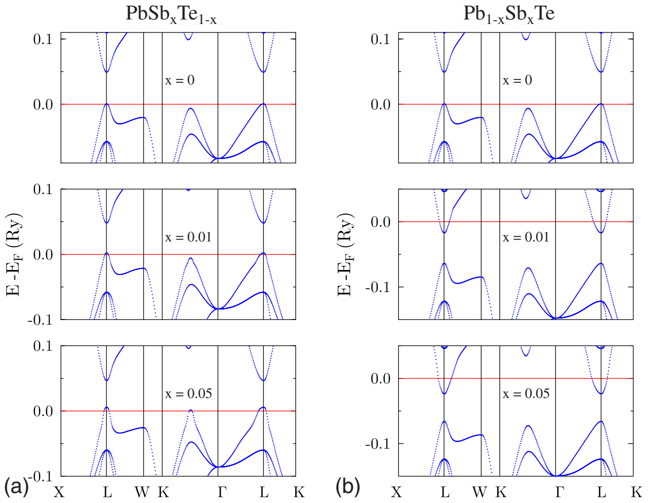

FIG. 4. (Color online) Calculated band structure near E_F of PbSb$_x$Te$_{1-x}$ (a) and Pb$_{1-x}$Sb$_x$Te (b) for increasing Sb concentration.

tellurium in quartz ampoules. The ampoules were sealed under vacuum and heated above the melting point of PbTe. The ampoules were quenched in water followed by a three week anneal at 773 K. Upon removal of the ingot from the ampoule, parallelepipeds measuring approximately $1\times1\times5$ mm^3 were cut using a diamond saw for galvanomagnetic and thermomagnetic measurements. Disks between 1.5–2.5 mm thick were cut for thermal flash diffusivity measurements. Coarsely powdered samples were used for the NMR measurements.

The ingots were polycrystalline and homogenous, with thermopower not varying by more than 2%–3% along either length of the ingot or across the diameter of the sectioned slices, indicating uniform carrier densities throughout the ingots. Powder x-ray diffraction did not indicate the presence of any second phase (Sb$_2$Te$_3$ in particular) at a concentration exceeding $\sim$1%. Further, the samples were tested in a differential scanning calorimeter over the temperature range of 303–823 K to test for phase changes and none were observed except in the cases explicitly described further.

Electrical resistivity (ρ) and Hall coefficient (R_H) were measured with an AC bridge while Seebeck (S) and isothermal transverse Nernst-Ettingshausen (N, further abbreviated to Nernst) coefficients were measured using the DC method with heater and sink in a conventional flow cryostat in the temperature range of 77–580 K. The magnetic field was stepped from -1.5 to 1.5 T at each temperature point. Any errors in Seebeck measurements are due to the inaccuracy in measuring the voltage and temperature at exactly the same point and we estimate them to be on the order of 3%. The error on the other quantities is dominated by uncertainties in the geometry of the sample; due to this we estimate errors of 5%. The two-carrier analysis presented in this article is dependent on transverse (Hall) resistance and on the magnetoresistance and thus encompasses errors present in both; assuming these errors are independent of each other, these quantities would be known to within about 7%. Further measurements of electrical resistivity, and Hall and Seebeck coefficients from 1.85–80 K were taken on a Physical Properties Measurement System by Quantum Design using the AC transport and thermal transport options. Errors on the resistivity and Hall coefficients are the same as stated for the 80–580 K range and errors on Seebeck are increased to 10% below 50 K due to the effect of the physical size of the Cernox thermometers on the accuracy of the measurement.

The thermal conductivity at the lower temperatures was measured using a static heater and sink method. When using this method above 250 K, heat losses may arise from thermal radiation. To address that issue, flash diffusivity measurements were taken on the Anter Corporation Flashline 3000 thermal diffusivity measurement system at room temperature and above. Specific heat was also calculated on this instrument using the comparative method relative to a standard stoichiometric PbTe reference sample, with results that were within the stated accuracy of 10% of the instrument as compared to reference data.[12] The thermal conductivity data from the static heater-and-sink and the flash diffusivity system match up well.

The nuclear magnetic resonance (NMR) experiments were performed at 126 MHz for ^{125}Te and 84 MHz for ^{207}Pb, on a Bruker Biospin (Billerica, MA) DSX-400 spectrometer (magnetic field of 9.39 T). The coarsely powdered samples were packed into plastic inserts with screw caps (from Bruker) that fit tightly into a 4 mm zirconia rotor. Using a magic-angle-spinning probe head (Bruker), the samples were rotated at 8 kHz, which narrowed the lines significantly. The $\pi/2$ pulse length was $\sim$3.5 μs. Signals were detected after saturation by 10 $\pi/2$ pulses and recovery followed by a Hahn echo generated by a $\pi/2-t_r-\pi$-t_r two-pulse sequence, where t_r denotes a rotation period. The π pulse and receiver phase were cycled according to the EXORCYCLE scheme.[13] Measuring times generally ranged between 1 and 15 h per spectrum, except for one spectrum as reported further, which required six days. ^{125}Te NMR chemical/Knight shifts were referenced to Te(OH)$_6$ in solution,[14] via solid TeO$_2$ at $+750$ ppm as a secondary reference. ^{207}Pb NMR chemical/Knight shifts were referenced to (CH$_4$)$_4$Pb in solution, via solid Pb(NO$_3$)$_2$ at -3500 ppm as a secondary reference.

IV. RESULTS AND DISCUSSION

A. Nuclear magnetic resonance

^{125}Te and ^{207}Pb NMR can identify the bonding environment of tellurium and lead nuclei via chemical shifts of the resonance frequencies. Even more importantly, NMR can be used to determine the carrier concentration of various regions within one sample by the Knight shift and spin-lattice relaxation time T_1, which are due to hyperfine coupling between the nuclear spin and polarized charge carriers.[15] One can distinguish between p- and n-type PbTe based on the opposite signs of their Knight shifts.[16] In ^{125}Te NMR, signals of n-type PbTe resonate to the left of, and p type to the right of, -1885 ppm,[17] and in ^{207}Pb NMR, analogously on either side of $+1300$ ppm. The absolute value of the carrier concentration can be determined over more than three orders of magnitude from the value of the T_1 relaxation time.[17,18] In order to remove the broadening by chemical or Knight-shift aniso-

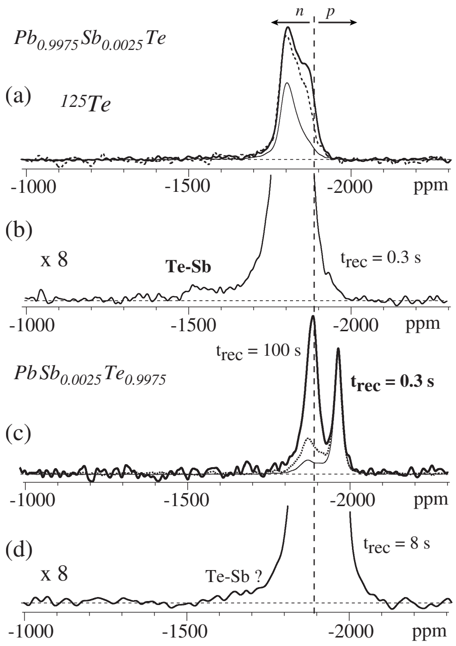

FIG. 5. ^{125}Te MAS NMR spectra of (a, b) $Pb_{0.9975}Sb_{0.0025}Te$ and (c, d) $PbSb_{0.0025}Te_{0.9975}$. (a) Spectra of $Pb_{0.9975}Sb_{0.0025}Te$ for various saturation-recovery delays. Thin line: 0.3 s; dashed line: 3 s; thick line: 10 s saturation-recovery delay (fully relaxed). (b) Spectrum with 0.3 s recovery delay shown with eightfold vertical expansion, which reveals the resonance of Te bonded to Sb at around −1530 ppm. (c) Spectra of $PbSb_{0.0025}Te_{0.9975}$ with 0.3 s (thin line), 1 s (dashed line), and 100 s recovery delay (thick line, fully relaxed). (d) Spectrum with 8 s recovery delay shown with eightfold vertical expansion. Measuring time: 6 days. The boundary between the Knight shifts of *n*- and *p*-type materials is indicated by a dashed vertical line.

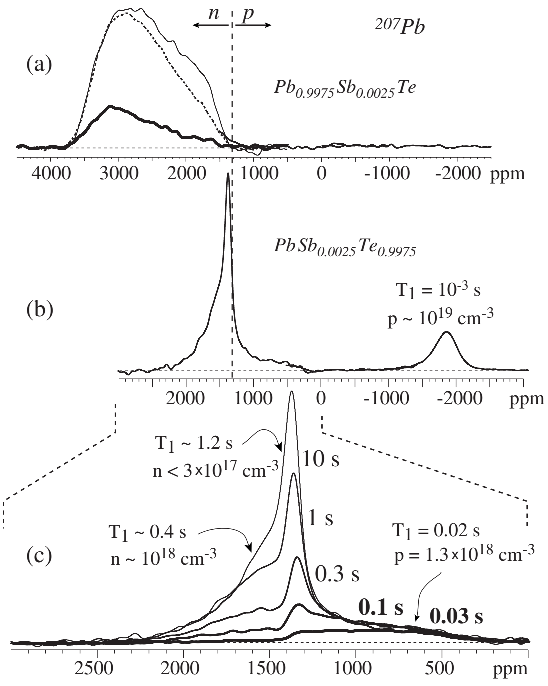

FIG. 6. ^{207}Pb MAS NMR spectra of (a) $Pb_{0.9975}Sb_{0.0025}Te$ and (b, c) $PbSb_{0.0025}Te_{0.9975}$. (a) Thin line: fully relaxed spectrum (1 s recycle delay). Dashed and thick lines: spectra with 0.3 and 0.03 s recycle delays, respectively. The right half of the spectrum, which does not show any signal, was acquired with 0.4 s recycle delay and irradiation at +400 ppm (center) and −1300 ppm (right). (b) Fully relaxed, composite spectrum of $PbSb_{0.0025}Te_{0.9975}$, measured with three different irradiation frequencies (+1300, −400, and −2100 ppm). (c) Partially relaxed spectra of $PbSb_{0.0025}Te_{0.9975}$, for the saturation-recovery delays given next to the spectra. The boundary between the Knight shifts of *n*- and *p*-type materials is indicated by a dashed vertical line.

tropy, spectra were measured with 8 kHz magic-angle spinning (MAS) of the sample.[19]

Figure 5 compares MAS ^{125}Te NMR spectra of $Pb_{0.9975}Sb_{0.0025}Te$ and $PbSb_{0.0025}Te_{0.9975}$. Spectra of $Pb_{0.9975}Sb_{0.0025}Te$ with 0.3 ms and 3 s recycle delays are compared in Fig. 5(a). Two components with different T_1 relaxation times (0.3 and 2.6 s) and frequency positions are recognized. The Knight shifts are characteristic of *n*-type PbTe, with the left short-T_1 component corresponding to the higher *n*. Figure 5(b) shows the 0.3 ms spectrum with eightfold expanded vertical scale. This reveals a small additional signal, chemically shifted by +250 ppm to around −1530 ppm, which is assigned to Te bonded to Sb,[17] confirming that Sb is incorporated into the Pb sublattice. The ^{125}Te spectra of $PbSb_{0.0025}Te_{0.9975}$ are drastically different, see Fig. 5(c). They show two resolved peaks with T_1 relaxation times differing by a factor of 40. The Knight shift and short relaxation time $T_1=0.11$ s of the right peak (−1965 ppm) are characteristic of a significant *p*-type carrier concentration. Figure 5(c) shows that the maximum of the broader left peak at ∼−1880 ppm shifts to the right with increasing recycle delay, indicating a distribution of moderate-to-low *n*-type carrier concentration. The vertically expanded spectrum in Fig. 5(d) shows little signal chemically shifted by ∼−250 ppm from the main PbTe peak, i.e., near −1650 ppm, corresponding to Te bonded to Sb, unlike the case in Fig. 5(b). The signal-to-noise ratio, limited by the long T_1 relaxation time, remained marginal even after six days of measurement. It is reasonable to conclude that even if a signal were present near −1650 ppm, the amount of Te bonded to Sb would be in a significantly lower concentration in $PbSb_{0.0025}Te_{0.9975}$ than in $Pb_{0.9975}Sb_{0.0025}Te$.

Figure 6 shows ^{207}Pb NMR spectra of $Pb_{0.9975}Sb_{0.0025}Te$ and $PbSb_{0.0025}Te_{0.9975}$. They show similar features as the corresponding ^{125}Te NMR spectra, but with higher resolution due to the ∼20-fold larger Knight shift of ^{207}Pb relative to ^{125}Te in PbTe.[16] The spectra of $Pb_{0.9975}Sb_{0.0025}Te$ in Fig. 6(a) match nicely with the corresponding ^{125}Te NMR spectra of Fig. 5(a) and confirm the presence of two main components with different Knight shifts and T_1 relaxation times, due to different *n*-type carrier concentrations. The measured ^{207}Pb T_1 relaxation times of 0.08 and 0.4 s can be converted to $n \sim 7 \times 10^{18}$ cm^3 and 1×10^{18} cm^3, respectively,[17,18] and are consistent with the ^{125}Te relaxation data. This matches with the Hall-effect data of $n \sim 9 \times 10^{18}$ cm^{-3}, as discussed in the next section. From the spectra and relaxation curves, the ratio of the components is near 60:40. The ^{207}Pb NMR spectra of $PbSb_{0.0025}Te_{0.9975}$ exhibit greater complexity, with at least four distinct components. The range of Knight shifts is so

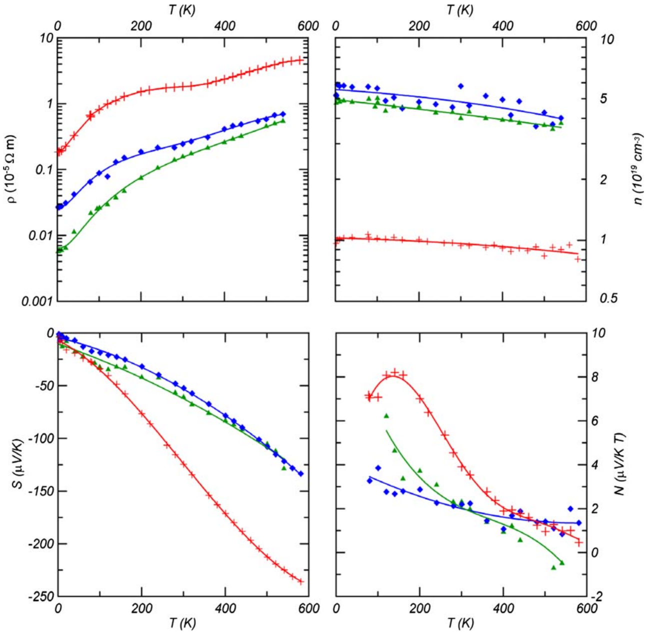

FIG. 7. (Color online) Resistivity, carrier concentration, Seebeck coefficient, and Nernst coefficient of *n*-type $Pb_{1-x}Sb_xTe$ samples. The symbols are: red plus – $Pb_{0.9975}Sb_{0.0025}Te$, green triangle – $Pb_{0.995}Sb_{0.005}Te$, and blue diamond – $PbS_{0.99}b_{0.01}Te$.

large (>4000 ppm) that the spectrum had to be obtained as a composite of measurements at different irradiation frequencies. As in ^{125}Te NMR, there is a sharp component with a *p*-type Knight shift (to the right at −1850 ppm) with a very short T_1 relaxation time of 1 ms, which corresponds to a high hole concentration of $p \sim (1 \text{ to } 2) \times 10^{19}$ cm^{-3}.[18] This accounts for ~20 to 40% of all Pb atoms. Another sharp peak, at +1370 ppm, with a Knight shift and long $T_1 \sim 1.2$ s characteristic of low electron concentration $n \leq 0.3 \times 10^{18}$ cm^{-3}, dominates the fully relaxed spectrum (~40% of all Pb); again, a corresponding peak had been identified in ^{125}Te NMR. A shoulder with intermediate T_1 ~0.4s and slight Knight shift to the left (at +1600 ppm) can be assigned to a moderate *n*-type carrier concentration, $n \sim 1 \times 10^{18}$ cm^{-3} (~25% of all Pb), while the broad resonance near +800 ppm with shorter $T_1 = 0.02$ s, see Fig. 6(c), must be attributed[18] to a moderate *p*-type carrier concentration $p = 1.3 \times 10^{18}$ cm^{-3} (~15% of all Pb). Four carriers types are thus identified by NMR, but only two of these ($p \sim 1.3 \times 10^{18}$ cm^{-3} and $n \sim 1 \times 10^{17} \leq 0.3 \times 10^{18}$ cm^{-3}) will be seen in the transport data that follow.

B. Transport in *n*-type $Pb_{1-x}Sb_xTe$

Galvanomagnetic and thermomagnetic data of materials in which Sb substitution is at the Pb site are shown in Fig. 7 as function of temperature at zero magnetic field. The Hall and Nernst coefficients reported are the slopes of the Hall resistance and Nernst voltages at zero field. The data in Fig. 7 are interpreted as follows.

All $Pb_{1-x}Sb_xTe$ samples are *n* type and degenerately doped, so that we assume the presence of only one type of carrier as indicated by NMR for $x = 0.25\%$. Under these circumstances, the carrier concentration is given by the Hall coefficient R_H using:[20]

$$n = r_H \frac{1}{R_H q} \tag{1}$$

where q is the electron charge and r_H is a prefactor that depends on the nature of the electron scattering mechanism. We assume, for simplicity, that the energy dependence of the relaxation time follows a power law:

$$\tau(E) = \tau_0 E^{\Lambda} \tag{2}$$

where μ is carrier mobility and Λ is the scattering exponent that takes the value of $-1/2$ for acoustic phonon scattering and 3/2 for ionized impurity scattering. For illustration purposes, in nondegenerately doped semiconductors, the Hall prefactor takes the values[20] of $r_H \sim 3\pi/8 \sim 1.18$ for acoustic phonon scattering and $r_H \sim 315\pi/512 \sim 1.93$ for ionized impurity scattering. When acoustic phonon scattering dominates, the Hall prefactor remains close to unity, but $r_H > 1$ when $\Lambda \gg 1$. The nature of the scattering mechanism and the value of Λ, can be deduced from the Nernst coefficient N. This fact is illustrated for the case of nondegenerately doped semiconductors where the Nernst coefficient is related to the scattering exponent by[20]

$$N = -(k_B/q)\mu\Lambda \tag{3}$$

where μ is carrier mobility. While we further use the full transport equations instead of Eq. (3) to derive quantitative information about Λ, the "method of the four coefficients,"[21] Eq. (3) provides a simple visual means to identify the nature of the scattering mechanism from a plot of the Nernst coefficient. Referring to Fig. 7, we see that N is small for all samples at temperatures above 300 K, with $x = 0.25\%$ having the largest Nernst. The values of N at $T > 300$ K indicate that acoustic phonon scattering dominates, and thus that $\Lambda \sim -1/2$ and $r_H \sim 1$. The increase in N as the temperature is lowered, particularly in the 0.25% sample, is due to the progressively increasing role of ionized impurity scattering at $T < 200$ K.

The carrier densities n represented in Fig. 7 are calculated from the measurements of R_H using Eq. (1) with $r_H = 1$. The reported values of n have a slight temperature dependence, due to the gradual change in the nature of the dominant scattering mechanism from acoustic phonon scattering at 500 K to ionized impurity scattering (i.e., $r_H(T)$ rather than the assumed value of 1). Therefore we can assume that n is temperature independent and has the value reported at 300 K. For $x = 0.25\%$ (or 3.7×10^{19} Sb atoms per cm^3), the carrier concentration is 9×10^{18} cm^{-3} at 500 K, corresponding to a doping efficiency of about 0.25 electrons per Sb atom. Increasing antimony content increases the carrier concentration, as expected, but it does not do so monotonically. With $x = 0.5\%$, $n(500 \text{ K}) \sim 3.7 \times 10^{19}$ cm^{-3}, corresponding to a 50% doping efficiency, but at $x = 1\%$, the doping efficiency falls back to about 0.3 electrons per Sb atom.

The electrical resistivity ρ of the samples is also shown in Fig. 7. We see an increase in resistivity with increasing temperature, which is metallic in nature. While the decrease in

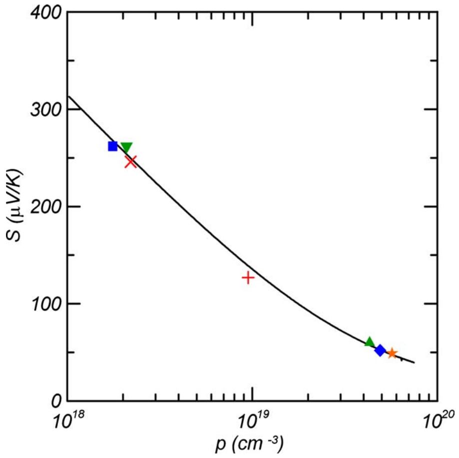

FIG. 8. (Color online) Absolute value of the thermopower vs carrier concentration ("Pisarenko relation") at 300 K. S is negative for electrons, positive for holes. The solid black line is the calculated thermopower for PbTe assuming acoustic phonon scattering; due to the high symmetry between conduction and valence bands, $|S(n)|$ is the same for both bands. The symbols are black X – $\mathrm{PbSb_{0.0025}Te_{0.9975}}$, green inverted triangle – $\mathrm{PbSb_{0.005}Te_{0.995}}$, blue square – $\mathrm{PbSb_{0.01}Te_{0.99}}$, red plus – $\mathrm{Pb_{0.9975}Sb_{0.0025}Te}$, green triangle – $\mathrm{Pb_{0.995}Sb_{0.005}Te}$, blue diamond – $\mathrm{Pb_{0.99}Sb_{0.01}Te}$, and orange star – $\mathrm{Pb_{0.98}Sb_{0.02}Te}$.

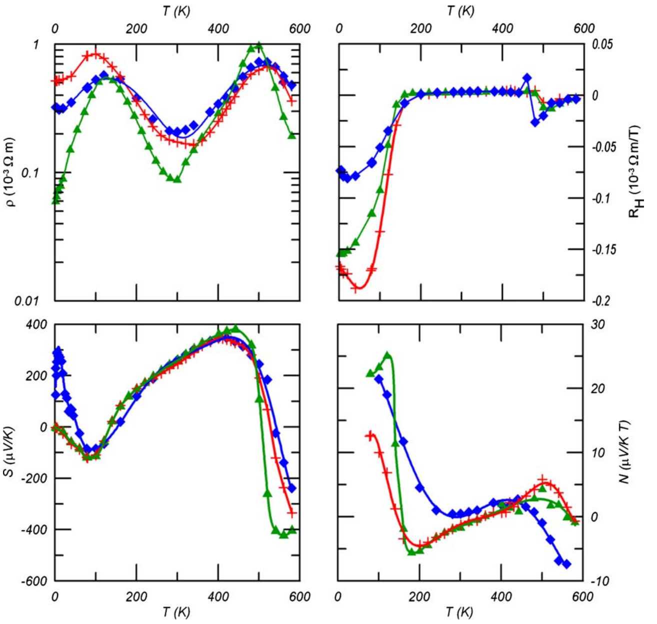

FIG. 9. (Color online) Resistivity, Hall, Seebeck, and Nernst coefficients of p-type $\mathrm{PbSb_xTe_{1-x}}$ samples. These traces are taken on the way up from cryogenic temperatures. The symbols are: red plus – $\mathrm{PbSb_{0.0025}Te_{0.9975}}$, green triangle – $\mathrm{PbSb_{0.005}Te_{0.995}}$, and blue diamond – $\mathrm{PbSb_{0.01}Te_{0.99}}$.

resistivity from $x=0.25\%$ to $x=0.5\%$ is due to the increasing carrier concentration, the increase in resistivity for $x=1\%$ over that of $x=0.5\%$ indicates an increase in scattering. To confirm this, we prepared an additional sample with $x=2\%$ that has a 300 K electrical resistance of $2.3\times10^{-6}\ \Omega\,\mathrm{m}$ (compared to $2.44\times10^{-6}\ \Omega\,\mathrm{m}$ for $x=1\%$) while it has slightly more carriers ($5.6\times10^{19}\ \mathrm{cm}^{-3}$ vs $4.9\times10^{19}\ \mathrm{cm}^{-3}$ for $x=1\%$). This confirms that the additional antimony acts as scattering centers. It is the balance between these ionized impurity and acoustic phonon scattering mechanisms that also leads to the shape of $\rho(T)$, which displays a broad "hump" around 150–200 K.

We see an almost linear increase in the Seebeck coefficient S with temperature at $T>200$ K as expected from the Mott relation for degenerate semiconductors. The $x=0.25\%$ sample shows signs of compensated behavior as the thermally excited holes begin to compensate the material at $T>500$ K. Plotted in Fig. 8 as a full line is the calculated "Pisarenko relation" $S(n)$ at 300 K. For carrier concentrations below $1\times10^{19}\ \mathrm{cm}^{-3}$, the calculated line is given for nondegenerate semiconductors by:[20]

$$S=\frac{k_B}{q}\left[\frac{5}{2}+\Lambda+\ln\frac{2(m_d^*k_BT/2\pi\hbar^2)^{3/2}}{n}\right] \tag{4}$$

with m_d^* the density of states effective mass; for higher carrier concentrations, S can be calculated from the full transport integrals,[21] and is slightly in excess of the value predicted by Eq. (4). The solid line in Fig. 8 is calculated with $\Lambda=-1/2$, and is quite well approximated by Eq. (4) below $1\times10^{19}\ \mathrm{cm}^{-3}$. Almost all room temperature experimental data points gathered for PbTe doped either n type or p type,[22] follow the calculated line, as do the samples studied here. PbTe has symmetry in the highest valence band and lowest conduction band, thus resulting in similar absolute values of thermopower for n-type and p-type samples with the same carrier concentrations. The data points shown are from samples in this study where the nonlocalized carriers, deduced from the Hall effect measurements, are plotted on the abscissas. Only the thermopower of samples in which there is a change in scattering parameter[23] or resonant energy level, such as in PbTe:Tl,[1] exceeds that line. We conclude from Fig. 8 that Sb does not form a resonant level at the concentrations studied here in spite of the sharpness of the maximum of the density of states calculated and shown in Fig. 2.

The low-temperature ($T<200$ K) Seebeck coefficient S of the higher antimony concentration samples does not extrapolate to zero at 0 K: the slight upturn probably originates from the increase in Seebeck coefficient that results from the ionized impurity scattering as the Λ term in Eq. (4) increases at low temperature.

C. Transport in p-type $\mathrm{PbSb_xTe_{1-x}}$

Figure 9 gives the galvanomagnetic and thermomagnetic data as measured for the samples with Sb on the Te site of nominal composition $\mathrm{PbSb_xTe_{1-x}}$ where $x=0.25\%$, 0.50%, and 1%. A phase transition is observed in these materials at ~525 K, which drastically and irreversibly changes the electronic properties. Samples heated to between 525 and 700 K and cooled again below 525 K stay n type. This change in the samples' condition between 500 and 550 K is metallurgical in nature and will not be addressed here further.

We discuss the Seebeck coefficient first. It is nearly linear with temperature from 240 to 400 K, though with a slight concave bend. If a straight line or tangent is drawn through these data we see that it will roughly intersect $S=0$ near $T=0$ K; this the behavior of a nearly degenerate semiconductor. In this regime the holes dominate the electrical properties of the material, which behaves like a degenerately doped p-type semiconductor with a temperature-independent hole concentration. Referring to Fig. 8, the thermopower vs carrier concentration for these samples falls on the line for the calculated Pisarenko relation at 300 K. As in the previous section, we conclude that Sb on the Te site does not create a resonant level in PbTe. Above the phase transition temperature, the Seebeck coefficient is negative due to the presence of electrons, and remains so upon subsequent cooling. Below 80 K, the Seebeck coefficient also becomes negative, but it turns positive again at the lowest temperatures and forms a large positive peak at $T<10$ K with a maximum near 6 K. We attribute the latter to phonon drag, but the fact that the peak is positive implies that holes are still present, in spite of the negative diffusion thermopower and the negative Hall coefficient. The Hall coefficient is much too large for the sample to have $p \sim 10^{19}$ cm^{-3} holes as one of the components seen by NMR, but the other electron and hole concentrations in NMR are on the order of $10^{18}-10^{17}$ cm^{-3}. NMR and the behavior of $S(T)$ suggest that the sample must have at least two, if not three different types of charge carriers. In order to limit the number of adjustable parameters, we will consider a two carrier regime, with one type of holes and one type of electrons.

In order to analyze the samples further, we measured the magnetoresistance $\rho_{xx}(B_z)$ and the transverse (Hall) resistivity $\rho_{xy}(B_z)$ as a function of magnetic field B_z from -1.5 to 1.5 T (raw data not shown). We invert the data to give the longitudinal $[\sigma_{xx}(B_z)]$ and transverse $[\sigma_{xy}(B_z)]$ conductivities:

$$\rho_{xx} = \frac{\sigma_{xx}}{\sigma_{xx}^2 + \sigma_{xy}^2} \quad \text{and} \quad \rho_{xy} = \frac{\sigma_{xy}}{\sigma_{xx}^2 + \sigma_{xy}^2} \tag{5}$$

and use the expressions for two-carrier conduction,

$$\sigma_{xx} = \frac{n \cdot q \cdot \mu_e}{1 + \mu_e^2 B_z^2} + \frac{p \cdot q \cdot \mu_h}{1 + \mu_h^2 B_z^2}$$

$$\sigma_{xy} = \frac{n \cdot q \cdot \mu_e^2 B_z}{1 + \mu_e^2 B_z^2} + \frac{p \cdot q \cdot \mu_h^2 B_z}{1 + \mu_h^2 B_z^2} \tag{6}$$

to derive the concentrations of the electrons (n) and holes (p) and their mobilities (μ_e, μ_h). In practice, Taylor series expansions were used around $B_z=0$ for magnetoresistance ($\Delta\rho/\rho$) and Hall coefficient as a function of magnetic field knowing that magnetoresistance is an even function and Hall is odd since the crystal has cubic symmetry. Fitting these at each temperature as a function of field yields n, p, μ_e, μ_h, and therefore the partial hole and electron conductivities at zero field:

$$\sigma_h = pq\mu_h, \quad \sigma_e = nq\mu_e, \quad \sigma = \sigma_h + \sigma_e. \tag{7}$$

The results of these fits are shown in Fig. 10 for one sample. The other two samples closely follow the behavior shown in Fig. 10 and are not included, for clarity. Furthermore, calculated data are not shown below 80 K due to the loss of numerical accuracy.

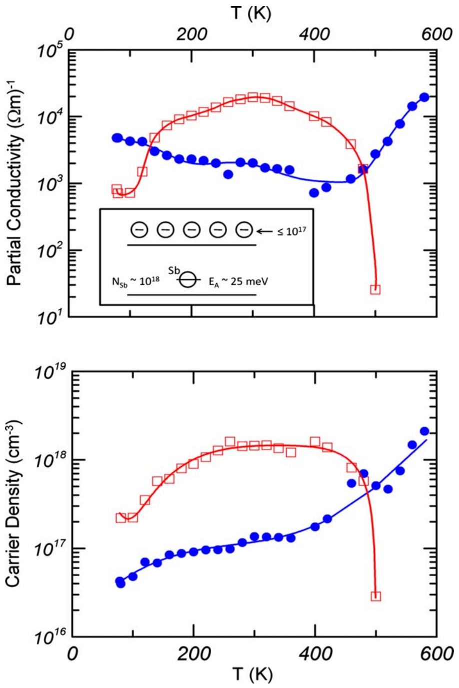

FIG. 10. (Color online) Partial conductivities and carrier concentrations as shown for a representative $PbSb_{0.005}Te_{0.995}$ sample. Blue filled circles are for electrons; red open boxes for holes. The conductivity and carrier concentration of the holes is not shown above 500 K as the samples become dominated by electrons and the data for the holes becomes incalculable. The insert shows a schematic diagram of the bands in $PbSb_xTe_{1-x}$, with a small ($\sim 10^{17}$ cm^{-3}) background concentration of electrons and a higher concentration of Sb atoms acting as acceptors with an ionization energy of ~ 25 meV.

Figure 10 makes it possible to derive the following model for $PbSb_xTe_{1-x}$, which is schematically represented as the bottom frame in the figure. At $T<525$ K, when most Sb atoms are not on the Pb sublattice and thus presumably substitute on the chalcogens sublattice, they are acceptors. The hole concentration from 80 to 500 K follows a $\ln(p) \propto T^{-1}$ law quite closely, with an activation energy of about 25 meV. The doping efficiency of Sb as an acceptor is not near unity, as 0.5 at. % Sb results in a saturated concentration of mobile holes of only 10^{18} cm^{-3}, or 1/40 of the concentration of Sb atoms. On top of these holes, the samples have a background concentration of mobile electrons of about $n \sim 1 \times 10^{17}$ cm^{-3} that is nearly temperature independent up to 400 K. Additionally, the concentration of holes is independent of Sb concentration. The ^{125}Te NMR spectrum Fig. 5(d) indicates that indeed a small amount of Sb atoms possibly may have Te neighbors and may thus reside on Pb sites, where they would act as donors.

The ^{207}Pb NMR spectra at 300 K of Fig. 6 showed four types of carriers: (1) a hole concentration of $p \sim (1 \text{ to } 2) \times 10^{19}$ cm^{-3} which we do not see contribute to transport, and (2) a second hole concentration of $p \sim 1.3 \times 10^{18}$ cm^{-3} which is mobile; (3) an electron concentration of $n \sim 1 \times 10^{18}$ cm^{-3}, which is not visible in transport, and (4) an electron concentration of $n \sim 1 \times 10^{17} \leq 0.3 \times 10^{18}\ \mathrm{cm}^{-3}$, which is also mobile. We represent the conclusions in the cartoon in Fig. 10 (inset). Sb has a *p*-type doping efficiency of 1 mobile hole (type 2) per 40 atoms, but the other (type 1) $p \sim 10^{19}$ carriers are localized; logically, these can be associated with the large peak in DOS in Fig. 3. The (type 4) mobile electrons might originate from the residual concentration of Sb atoms that are on the Pb sites in spite of the Te deficiency of the samples, while the (type 3) $n \sim 10^{18}\ \mathrm{cm}^{-3}$ are also localized. This model leads to one more very important conclusion. It has been mentioned often in the thermoelectric literature that a peak in the DOS should lead to a strong increase in the Seebeck coefficient exceeding the Pisarenko relation. While this is a necessary condition, it is not a sufficient one, as is illustrated here by comparing Figs. 3 and 8. Indeed, the Mott relation which underlies the enhancement of $S(p)$ reads:[24]

$$S = \frac{\pi^2}{3}\frac{k_B}{q}(k_B T)\frac{1}{\sigma(E)}\left(\frac{d\sigma(E)}{dE}\right)_{E=E_F} = \frac{\pi^2}{3}\frac{k_B}{q}(k_B T)\left(\frac{1}{g}\frac{dg}{dE} + \frac{1}{\mu}\frac{d\mu}{dE}\right) \qquad (8)$$

where $\sigma(E)$ is the partial electrical conductivity of a carrier at energy E, and $g(E)$ is thus the density of *delocalized* states of energy between E and $E+dE$. States that have a localized character do of course not contribute to conduction or thermopower. In this context, we point out that it has been demonstrated that in a given solid, a state at energy E must be either localized or delocalized.[25]

This model for $\mathrm{PbSb_xTe_{1-x}}$ allows us to explain the other transport properties. The Seebeck and Hall coefficients are negative around liquid nitrogen temperature, because they both are weighted averages between the partial Seebeck coefficients of electrons and holes, weighted by the partial conductivities (or mobilities square, for the Hall coefficient). As shown in Fig. 10, the partial conductivity of the holes at 80 K is an order of magnitude lower than that of electrons, thus driving the Seebeck coefficient negative. Additionally, the positive phonon drag peak in the Seebeck coefficient is thus explained due to the higher concentration of holes than electrons at low temperatures. The Nernst coefficient for two-carrier systems is a function not only of the partial Nernst coefficients of electrons and holes, but also contains a term that is proportional to the difference between the partial electron and hole Seebeck coefficients.[20] In systems that contain both electrons and holes, these Seebeck terms add and become dominant, leading to the very high values at $T < 150$ K reported in Fig. 9.

The electrical resistivity curves for all three samples follow the same trends, having peaks at 125 K and at 500 K. Starting from the lowest temperatures, conduction below 100 K is dominated by the more mobile electron, and phonon scattering results in a positive temperature dependence of ρ. The negative slope of $\rho(T)$ after the first peak is due to the thermal activation of the antimony acceptors forming holes in the valence band. The resistivity drops until it bottoms at 300 K, where the activation of the acceptors is saturated and phonon scattering of the carriers imparts a positive slope to $\rho(T > 300\ \mathrm{K})$. The second peak occurs in the temperature region of the phase transition. The rapid drop of the Seebeck coefficient at temperatures exceeding 500 K is related to a phase transition, whereby a fraction of the antimony presumably leaves the tellurium sites and looses its acceptor action. When cooled back below 520 K, samples remain permanently *n*-type.

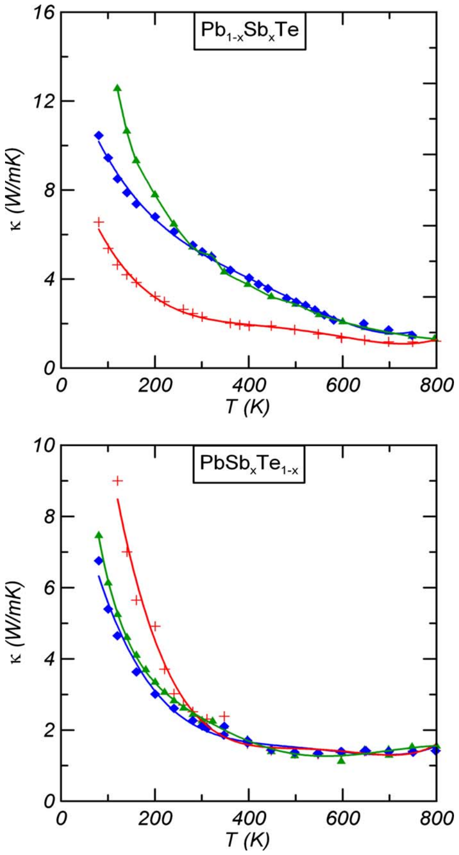

FIG. 11. (Color online) Thermal conductivities for the samples in this study. The symbols are: red plus - 0.25% Sb, green triangle – 0.5% Sb, and blue diamond – 1% Sb.

D. Thermal conductivity

Thermal conductivity data of both $\mathrm{Pb_{1-x}Sb_xTe}$ and $\mathrm{PbSb_xTe_{1-x}}$ are shown in Fig. 11. There is an increase in thermal conductivity of $\mathrm{Pb_{1-x}Sb_xTe}$ with increasing x due to increased electronic thermal conductivity. The $x=1\%$ sample has a lower thermal conductivity at low temperatures than the $x=0.5\%$ sample, which is presumed to be due to alloy scattering, while the high temperature values are almost equivalent from the balance of a slightly increased electronic thermal conductivity term with a decreased lattice thermal conductivity. The $x=0.25\%$ sample has lower thermal conductivity over all temperatures, which results from its higher electrical resistivity.

The thermal conductivity of $\mathrm{PbSb_xTe_{1-x}}$ is shown in the bottom half of Fig. 11. The conductivities for the three samples are approximately equal above 300 K, with differences at lower temperatures attributed to increased alloy scattering with increasing Sb content. At the concentrations of impurities studied here, we see that the usage of alloy scattering to lower-lattice thermal conductivity is limited to low temperatures and does not have any discernable effect on higher temperature thermal conductivity, as witnessed in samples that have similar electronic thermal conductivities.

V. CONCLUSIONS

In this study we investigated the role that Sb takes on both the metal and chalcogen lattice positions in PbTe. Band structure calculations were confirmed in their predictions that Sb is an amphoteric dopant depending on lattice position. In Te-rich PbTe, Sb fills the Pb lattice position, as confirmed by NMR, with doping efficiencies between 0.3–0.5 in low-doped samples and a decreasing efficiency with increasing Sb. In Pb-rich samples prepared by quenching from the melt, most Sb atoms fill the Te site and far fewer Sb-Te bonds are seen by NMR. NMR also reveals four types of carriers, a high concentration of holes that do not contribute to conduction, about 10^{18} cm^{-3} mobile holes with a thermal activation energy of 25 meV from transport data, about the same concentration of localized electrons, and an order of magnitude lower concentration of mobile electrons. The 10^{18} cm^{-3} mobile holes do not depend on the amount of Sb introduced in the samples, suggesting that there is a limited solubility of Sb on the Te site in Pb-rich PbTe. Heating the Pb-rich samples above 525 K results in an irreversible metallurgical phase transition.

Work by C.M.J. and J.P.H. was supported by BSST, LLC, and partially by the Ohio Department of Development WCI grant on Photovoltaic Innovation and Commercialization. J.T. acknowledges the partial support of the Polish Ministry of Science and Higher Education under the grant No. N202-2104-33. Work by E.M.L. and K.S.R. was supported by the U.S. Department of Energy—Basic Energy Sciences under Contract No. DE-AC02-07CH11358.

---

[1] J. P. Heremans, V. Jovovic, E. S. Toberer, A. Saramat, K. Kurosaki, A. Charoenphakdee, S. Yamanaka, and G. J. Snyder, Science **321**, 554 (2008).

[2] K. F. Hsu, S. Loo, F. Guo, W. Chen, J. S. Dyck, C. Uher, T. Hogan, E. K. Polychroniadis, and M. G. Kanatzidis, Science **303**, 818 (2004).

[3] J. R. Sootsman, H. Kong, C. Uher, J. J. D'Angelo, C. I. Wu, T. Hogan, T. Caillat, and M. G. Kanatzidis, Angew. Chem. Int. Ed. **47**(45), 8618 (2008).

[4] A. J. Strauss, J. Electron. Mater. **2**, 553 (1973).

[5] N. K. Abrikosov, E. V. Skudnova, L. V. Poretskaya, and T. A. Osipova, Inorg. Mater. **5**, 630 (1969).

[6] A. Bansil, S. Kaprzyk, P. E. Mijnarends, and J. Tobola, Phys. Rev. B **60**, 13396 (1999).

[7] T. S. Stopa, J. Kaprzyk, and J. Tobola, J. Phys.: Condens. Matter **16**, 4921 (2004).

[8] R. Dalven, Infrared Phys. Technol. **9**, 141 (1969).

[9] S. Kaprzyk and A. Bansil, Phys. Rev. B **42**, 7358 (1990).

[10] M. Lach-hab, D. A. Papaconstantopoulos, and M. J. Mehl, J. Phys. Chem. Solids **63**, 833 (2002) and references therein.

[11] S.-H. Wei and A. Zunger, Phys. Rev. B **55**, 13605 (1997).

[12] A. Pashinkin, V. Zlomanov, and A. Malkova, Inorg. Mater. **30**, 1118 (1994).

[13] G. Bodenhausen, R. Freeman, and D. L. Turner, J. Magn. Reson. **27**, 511 (1977).

[14] I. Orion, J. Rocha, S. Jobic, V. Abadie, R. Brec, C. Fernandez, and J.-P. Amoureux, J. Chem. Soc., Dalton Trans. 1997, 3741.

[15] C. P. Slichter, *Principles of Magnetic Resonance* 3rd Ed, (1990).

[16] D. Senturia, A. C. Smith, C. R. Hewes, J. A. Hoffmann, and P. L. Sagalyn, Phys. Rev. B **1**, 4045 (1970).

[17] E. M. Levin, B. A. Cook, K. Ahn, M. G. Kanatzidis, and K. Schmidt-Rohr, Phys. Rev. B **80**, 115211 (2009).

[18] M. N. Alexander, P. L. Sagalyn, S. D. Senturia, and C. R. Hewes, J. Nonmet. **1**, 251 (1973).

[19] K. Schmidt-Rohr and H. W. Spiess, *Multidimensional Solid-State NMR and Polymers* (Academic Press, London, San Diego, 1994).

[20] F. J. Blatt, *Physics of electronic conduction in solids* (McGraw-Hill, New York, 1968).

[21] J. P. Heremans, C. M. Thrush, and D. T. Morelli, Phys. Rev. B **70**, 115334 (2004).

[22] S. V. Airapetyants, M. N. Vinogradova, I. N. Dubrovskaya, N. V. Kolomoets, and I. M. Rudnik, Sov. Phys. Solid State **8**, 1069 (1966).

[23] J. P. Heremans, C. M. Thrush, and D. T. Morelli, J. Appl. Phys. **98**, 063703 (2005).

[24] M. Cutler and N. F. Mott, Phys. Rev. **181**, 1336 (1969).

[25] M. H. Cohen, Can. J. Chem. **55**, 1906 (1977).